

Die Grenzen der
Chemie neu ausloten?
It takes
#HumanChemistry

Wir suchen kreative Chemikerinnen und Chemiker,
die mit uns gemeinsam neue Wege gehen wollen –
mit Fachwissen, Unternehmertum und Kreativität für
innovative Lösungen. Informieren Sie sich unter:

[evonik.de/karriere](https://www.evonik.de/karriere)

On the Morphological and Crystallographic Anisotropy of Diesel Particulate Filter Materials

Fabien Léonard, Axel Lange, Andreas Kupsch, Bernd Randolph Müller, and Giovanni Bruno*

The determination of the anisotropy of materials' microstructure and morphology (pore space) in diesel particulate filter (DPF) materials is an important problem to solve, since such anisotropy determines the mechanical, thermal, and filtration properties of such materials. Through the use of a dedicated (and simple) segmentation algorithm, it is shown how to exploit the information yielded by 3D X-ray computed tomography data to quantify the morphological anisotropy. It is also correlated that such anisotropy of the pore space is also correlated with the microstructure and crystallographic anisotropy of the material in several showcases: a microstructurally isotropic material, such as SiC, and some morphologically and microstructurally anisotropic cordierite materials. In the later case, the finer the grain size, the more isotropic the microstructure.

(i.e., reaction-driven phase formation) at high temperature.^[2] This extrusion process causes anisotropy at both microscopic (grains and pores) and macroscopic (properties) level.^[3] In other words, the crystallographic (grain orientation), the microstructural (grain shape), the morphological (pore orientation), and the material's properties (mechanical, thermal, and filtration) acquire a preferential orientation along the extrusion axis. This orientation dependence extends at to the component level, and is exacerbated by the cellular geometry of the filter (cells are oriented along the extrusion axis, too).

Indeed, a dependence of materials' properties on direction has been reported at

component level (Young's modulus and thermal expansion,^[3,4] and at material level (CTE,^[4,5] fracture toughness,^[6] and stress-strain curves^[7]). Recently, an analysis of both X-ray refraction and computed tomography images^[8] has shown that the orientation of the porosity is directly correlated with the anisotropy of the mechanical and thermal properties.

Importantly, we must refrain from talking about "pores," because the porosity in these materials is totally interconnected. It is therefore impossible to analyze porosity by reducing the problem to "unit cells" containing voids of defined geometry (as typically done in the literature^[9]). Instead, we need to consider approaches that tackle the problem of determining *global* (mechanical and thermal) properties of the material, including its pore space (called *porosity* within this paper, not to confuse with the porosity fraction p).

While the microstructure of these materials has been classically investigated by means of scanning electron microscopy (see, e.g.,^[6a,10]), since the resolution needed lies within the realm of SEM, a global view of the microstructure is also needed, yet with the highest possible resolution. Optical microscopy (OM) can yield relevant information and is used in industrial research, but is a 2D technique and lacks resolution. On the contrary, X-ray computed tomography (XCT) has the potential to disclose features in the bulk (3D analysis), with a resolution intermediate between SEM and OM, and a large field of view, comparable with OM. One disadvantage of XCT is that, the images being reconstructions (as opposed to direct acquisitions in microscopy), retrieval of objects and features may require particular expertise, and is not a trivial task. In other words, what can appear clear to the human eye in an XCT reconstruction may not be quantifiable and may be an artefact (this sometimes similarly happens in microscopy). Therefore, image processing and computer codes are needed to extract quantitative information from CT reconstructions.

1. Introduction

Diesel Particulate Filter (DPF) materials are usually porous ceramics, often containing microcracks.^[1] The reasons for this choice are manifold: 1) they can be used at very high temperatures (in excess of 1000 °C); 2) they have very good thermal shock resistance in their temperature range of application (especially if microcracked), i.e., 600–900 °C; 3) they are inert to many gases and combustion products in a large temperature range (typically even exceeding 1100 °C); and 4) they can be manufactured with tailored porosity (amount and size distribution).

The usual way of DPF production consists of the extrusion of a slurry into the desired filter shape, with successive firing


F. Léonard, A. Lange[†], A. Kupsch, B. R. Müller, G. Bruno
Bundesanstalt für Materialforschung und -prüfung
Unter den Eichen 87, 12205 Berlin, Germany
E-mail: giovanni.bruno@bam.de

F. Léonard

The University of Manchester at Harwell
Harwell Campus, Didcot, Oxfordshire OX11 0DE, UK

G. Bruno

Institute of Physics and Astronomy
University of Potsdam
Karl-Liebknecht-Str.24-25, 14467 Potsdam, Germany

 The ORCID identification number(s) for the author(s) of this article can be found under <https://doi.org/10.1002/adem.202101380>.

© 2021 The Authors. Advanced Engineering Materials published by Wiley-VCH GmbH. This is an open access article under the terms of the Creative Commons Attribution License, which permits use, distribution and reproduction in any medium, provided the original work is properly cited.

[†]Deceased author.

DOI: 10.1002/adem.202101380

Statistical methods (autocorrelation function and permeability calculations^[11] or two point correlation function calculations^[12]) have been applied to XCT reconstructions in order to extract the orientation of the permeability and of the pore morphology tensors. Such methods are fully 3D, but require a certain computational effort and are sensitive to the choice of some calculation parameters. For some applications, such as the case of DPFs, where the axes of anisotropy are approximately known a priori (because of the extrusion process), it is preferable or anyway faster to use 2D methods, which work on single reconstructed slices (note that some reconstruction programs do work on single slices).

This kind of global approaches has the great advantage of being directly comparable with analytical and numerical global models, designed to extract or predict mechanical or thermal properties (also leveraging on the equivalence of such properties for calculation purposes). They also compare well with measurements at the mesoscale, such as those made by 2D X-ray refraction techniques^[8c,13], which have been proven to be able to quantitatively estimate the anisotropy of ceramic materials.

Finally, it is to be noted that Kachanov and Sevostianov^[14] have indicated that from a theoretical point of view, the orthorhombic symmetry of the crystals (cordierite and aluminum titanate, the most typical materials for DPFs, have orthorhombic crystal symmetry^[15]) does imply orthotropic geometry and (mechanical and thermal) property symmetry. We therefore compare anisotropic (cordierite, orthorhombic crystal structure) and isotropic (silicon carbide, α -SiC, and hexagonal crystal structure) microstructures, possessing similar porosity fraction but different materials properties, and determine their morphological anisotropy tensors as well as their correlation with the crystallographic texture.

2. Characterization and Analysis Methods

2.1. X-Ray Computed Tomography

X-ray computed tomography is a nondestructive imaging technique based on differences in X-ray absorption from the multiple constituents of a specimen (different materials and/or different features, such as inclusions, pores, cracks, and matrix). The specimen is placed between an X-ray source and an X-ray detector, then rotated so that a series of 2D radiographic images (usually thousands) can be acquired over a full 360° rotation of the specimen. These 2D radiographic images are then processed so that a 3D digital reconstruction of the specimen can be obtained. The reconstructed volume is a 3D image composed of voxels, the 3D equivalent of a pixel in a 2D image, which contains a gray value that is representative of the local linear attenuation coefficient over the corresponding sampled volume within the specimen. Therefore, to be able to resolve a certain feature, two conditions are required: first, the feature must be significantly larger than the voxel size of the reconstructed volume and second, there should be enough contrast in the gray values corresponding to the different features of interest.

2.1.1. Laboratory X-Ray Computed Tomography

Laboratory XCT experiments were performed on a GE v|tome|x L 300/180 equipped with a 180 kV source, a tungsten transmission target (actual focal spot size below 2 μm as determined with JIMA

test pattern RTC02), and a GE 2000 \times 2000 pixel DXR-250 detector. The source was operated at a voltage of 60 kV and a current of 170 μA . The sample projections were taken at 1500 angular positions per 360° rotation, with increments of 0.24°, and an exposure time of 3 s. The samples were placed 8 mm from the source, with a source-detector distance of 800 mm, and a binning of 2 \times 2 pixels, so that the effective magnification was 50 (field of view of 4 \times 4 mm²). The resulting voxel size was 4.0 μm and the scan time 1 h 15 min. In order to ensure the imaging of the entire sample, pieces of 2 \times 2 cells were cut out of the honeycomb assemblies.

2.1.2. Synchrotron Radiation X-Ray Computed Tomography

Synchrotron-XCT (SXCT) measurements were performed at the beamline BAMline^[16] at the synchrotron source BESSY II of the Helmholtz-Zentrum Berlin für Materialien und Energie (HZB), Berlin, Germany. The beam energy was set to 15 keV, in order to achieve optimal contrast for the investigated porous filter structures. A PCO4000 CCD camera (4008 \times 2672 pixels) was used in combination with an Optique Peter microscope equipped with a CdWO₄ scintillator and a 10-fold magnifying objective, resulting in a pixel size of 0.434 μm . A series of 3200 projections were acquired per 180° rotation, with a 4 s exposure. A small sample-detector distance of 15 mm was set to ensure a limited scattering range of refractive edge artifacts (also called phase contrast in the literature), and the entrance slits were narrowed to a field of view (FoV) of 1.7 \times 1.1 mm² to avoid detector backlighting.^[17,18] In order to avoid the sample size exceeding the FoV, small splinters of less than 1.5 mm size were prepared from each sample, containing just one crossing region and one protruding wall.

2.2. Directional Interface Variance Analysis (DIVA)

The DIVA methodology, for directional interface variance analysis, is based on the analysis of the variance of the absolute value of the gradients of the X-ray attenuation coefficient on a 1D projection of each slice of the 3D XCT data set. The procedure has been described in details in.^[8b] Herewith, we report its salient features, which are illustrated in **Figure 1**.

The DIVA takes the projection of the *gradient's* $\nabla\mu$ absolute of the image along different directions

$$P_\varphi(\xi) = \int_V |\nabla\mu(\eta, \xi)| d\eta \quad (1)$$

where P_φ is the 1D projection along η , which is tilted by an angle φ from the y axis in the laboratory co-ordinate system ($\eta = -x \sin(\varphi) + y \cos(\varphi)$), $\mu(x, y)$ is the spatial distribution of the attenuation coefficient (i.e., the 2D XCT slice of the object), and calculates its variance

$$\sigma_P^2(\varphi) = \left[\sum_{\xi_i}^n (P_\varphi(\xi_i) - \langle P_\varphi \rangle)^2 \right] / n \quad (2)$$

where the average operator is run over the spatial co-ordinate $\xi = x \cos(\varphi) + y \sin(\varphi)$, which must be thought as a discrete variable, since the projection is acquired by a detector with discrete pixels (see **Figure 1**), and n the number of pixels.

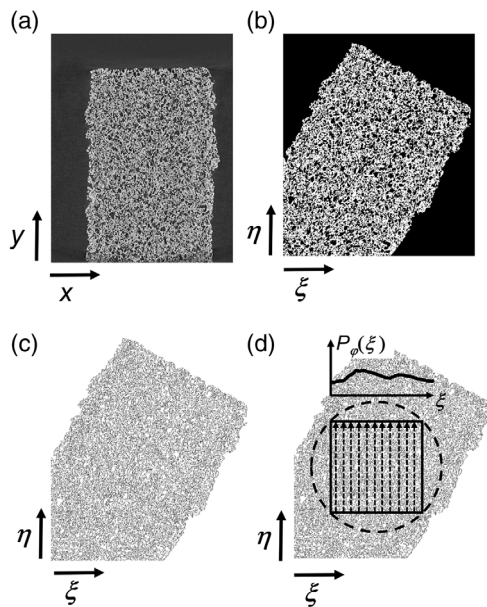


Figure 1. Principle of DIVA processing steps (see also^[8b]). A slice $\mu(x,y)$ of the reconstructed volume a) is rotated by an angle φ and binarized, b). The absolute value of the gradient $|\nabla\mu|$ is computed c). The projection along η results in the profile $P_\varphi(\xi)$ d). Interfaces parallel to η result in locally high signals, whereas interfaces parallel to ξ result in small broad contributions to $P_\varphi(\xi)$. Thus, the variance of $P_\varphi(\xi)$ is the higher, the more interfaces parallel to η are present.

It then calculates the ratio of the variances of two perpendicular projections for each projection angle φ , thereby calculating an anisotropy ratio at each tilt angle φ .

This allows determining the orientation (angular) distribution of the global porosity (i.e., the edges of the dense material) of one single slice by plotting the ratio of the variances in two perpendicular directions (i.e., the orientation parameter O_D) versus the polar angle φ , whereby

$$O_D = \frac{\sigma_p^2(\varphi)}{\sigma_p^2(\varphi + \frac{\pi}{2})} \quad (3)$$

This distribution yields the maximum, $\max(O_D)$, and the direction $\varphi(\max(O_D))$, at which the maximum occurs. The O_D represents the ratio of the amounts of material–air interfaces in two perpendicular directions. The quantity $\max(O_D)$ can be seen as the aspect ratio of the elliptical pore equivalent to all the interfaces (“pores”) present in the slice. If $\max(O_D) = 1$, the “pores” are randomly oriented, while for well aligned crack-like pores $\max(O_D)$ can reach high values, though never infinite, since the thickness of the “cracks” cannot be zero. In this respect, $\max(O_D)$ is fully equivalent to a crystallographic texture index.

Applying this procedure to a large number of slices (all having one pixel thickness) throughout the sample, one can calculate thickness-dependent 1D pole figures (in one particular sample direction). Alternatively, one can stack the images together in order to calculate an average orientation distribution (1D pole figure) in the plane of the slices, and a global O_D . This procedure can be repeated in three perpendicular planes, and three 1D pole figures (and three

Table 1. Overview of DPF samples under investigation. p is the porosity fraction obtained either through mercury porosimetry measurements (p - Hg) or from the XCT images (p - XCT).

Material	p - Hg [%]	p - XCT [%]	Pixel size in image [μm]
Cord_1	52	48	4.0
Cord_2	48	50	4.0
Cord_31	50	48–50	0.434
Cord_32	50	48–50	0.434
Cord_41	65	62	0.434
Cord_42	65	62	0.434
SiC	48	50	0.434

$\max(O_D)$) can be extracted, yielding a hint of the size and orientation of the ellipsoid corresponding to the pore morphology tensor.

By its own construction (ratio between projection variances in two perpendicular orientations), DIVA cannot be fully 3D. Nevertheless, the projection of the orientation ellipsoid in the three principal planes of the sample already gives a good idea of the orientation of the pore space in the cases where some prior knowledge about the anisotropy can be used (in this case, we know that the DPFs are extruded in the z direction).

3. Diesel Particulate Filter Materials

A total of 5 materials have been investigated, four are cordierites (labelled Cord_1 to _4) and one is SiC; an overview of the samples is given in Table 1.

Cordierite materials were provided by Corning Incorporated (Corning, NY, USA) and Oak Ridge National Laboratory (Oak Ridge, TN, USA). All of them are extracted from monolithic filters, all produced by the extrusion process mentioned above. Cordierite raw materials consisted of SiO_2 , MgO , hydrated Al_2O_3 , and $\text{Al}_2\text{-Si}_2\text{O}_5(\text{OH})_4$ (Caolin). Different porosities were achieved by adding different amounts of pore formers. Firing was made at temperatures in excess of 1300°C , with successive cooling at rates below 1°C min^{-1} in N_2 -enriched air. The SiC filter materials were commercially available (manufacturer NGK, Japan). The porosity fraction was determined by mercury intrusion with an Autopore 6520 Micromeritics, Norcross, USA. Porosity values are reported in Table 1, together with the results of image analysis of computed tomography data (see below) (note that by mercury porosimetry one can also extract a pore size distribution and a median pore size, but we consider such number invalid for bi-continuous media, such as DPFs, see also^[19]).

4. Results

4.1. X-Ray Computed Tomography

Cordierite specimens Cord_1 and Cord_2 were scanned on a laboratory CT system whereas samples Cord_3w, Cord_4w ($w = 1,2$) and SiC were scanned on the synchrotron beamline BAMline, BESSY II, HZB Berlin, Germany. Some 2D XCT slices from all samples are gathered in Figure 2.

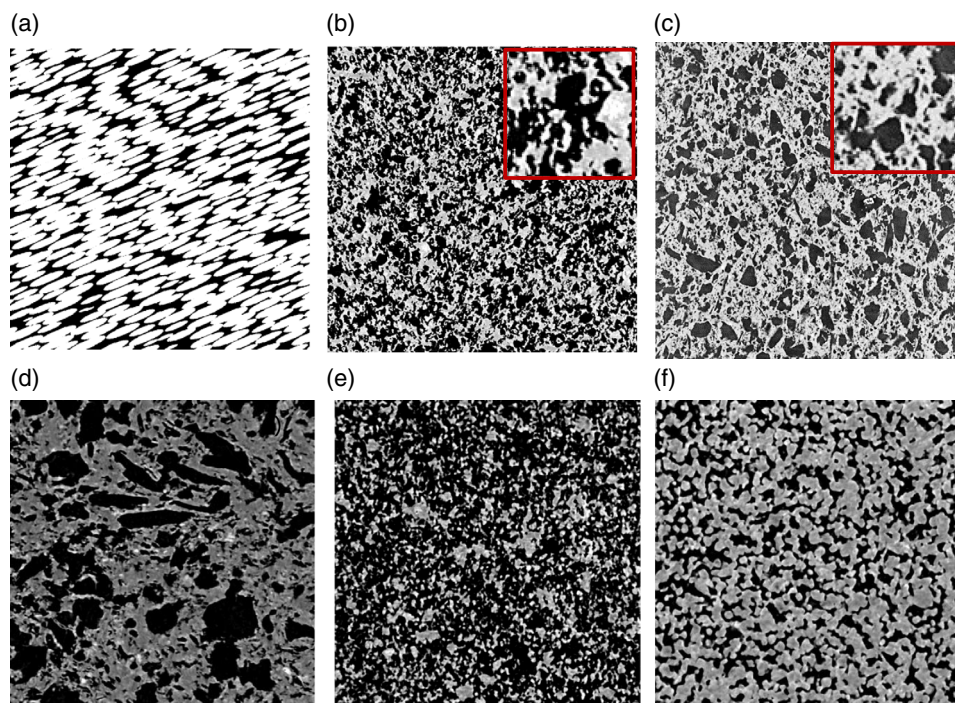


Figure 2. Overview of DPF samples under investigation. a) Simulated data: image size 1000×1000 pixels (porosity fraction = 0.33); b) Cord_1: Image size 2.18×2.18 mm², inset size 0.31×0.31 mm²; c) Cord_2: Image size 2.18×2.18 mm², inset size 0.31×0.31 mm²; d) Cord_3: Image size 0.31×0.31 mm²; e) Cord_4: Image size 0.31×0.31 mm²; f) SiC: Image size 0.31×0.31 mm².

For comparison purposes, slices of Cord_1 and Cord_2 carry an inset with the same resolution as slices of Cord_3, Cord_4, and SiC. We observe large differences in pore sizes between Cord_3 and Cord_4.

Qualitatively, Cord_1, Cord_2, and Cord_3 are similar materials, and show similar porosity features: “pores” (intended as the objects visible in the XCT slices) are sharp-edged and have a large size distribution; on the contrary, Cord_4 possesses much smoother pore/material interfaces and a larger porosity fraction. For SiC (Figure 2f), footprints of the powder particles composing the final material are clearly visible; correspondingly, the “pores” have a rounded shape. This is also confirmed by the analysis carried out by Bruno et al.^[20] on the base of the work by Roberts and Garboczi,^[9b] where this very same SiC material^[9b] was found to possess the mechanical behavior of a bi-continuous solid formed by sintering of solid spheres. The nominal total porosity in SiC should have been lower than that of cordierite samples Cord_1, Cord_2, and Cord_3, but it resulted to be only marginally lower.

Interestingly, the homogeneity of the pore space (the “pores” visible in the XCT slices) is higher for SiC and Cord_4 than for Cord_1 to Cord_3 samples. For SiC, this is due to the fact that the SiC sample was most probably manufactured using sieved powder (i.e., with a narrow particle size distribution). For cordierite, the matter is more complicated, since both pore former particles and initial raw materials (powder particle distributions) play a role. No clear global orientation of the pore space is visible from the XCT slices.

Figure 3 shows 3D reconstructions of Cord_1 sample (b) and the images corresponding to the procedure for data preprocessing before DIVA analysis (c and d, see figure caption). In order to be

consistent, all the specimens were first aligned with the processing axes, then a subvolume fully contained within the filter walls was extracted. For Cord_3 and Cord_4, two different subvolumes were extracted from two perpendicular walls. In all cases, however, the reference coordinate system was defined as: A along the wall length (in red), B the extrusion direction (in green), and C normal to the wall (in blue). This nomenclature will be conserved throughout the paper to allow an easier comparison among samples with different relative orientations within the filter.

4.2. DIVA

To better understand the capabilities of the DIVA analysis, a calculation example was performed on a simulated data set of a dense packing of ellipsoidal particles. Details about the simulated data set can be found in^[11] and are summarized here: the starting point was a random close packing of 10^5 nonoverlapping spheres placed within a unit cube (edges equal to one) and having the same density and diameter.

The positions of the sphere centres were modified by dividing the B coordinate (green axis Figure 4a) by 2, and the C coordinate (blue axis) by 10. Then an ellipsoidal particle (Figure 4b) was placed at each modified centre and a rotation of 23° around the A axis (red axis) applied. Finally, the discrete binary image ($10\,003$ voxels) presented in Figure 4b was generated from the central region of this ellipsoids packing. In the resulting simulated volume, all particles are the same (geometry and density) and identically oriented; there is no overlap between particles, and all distances between near neighbors are different (because of

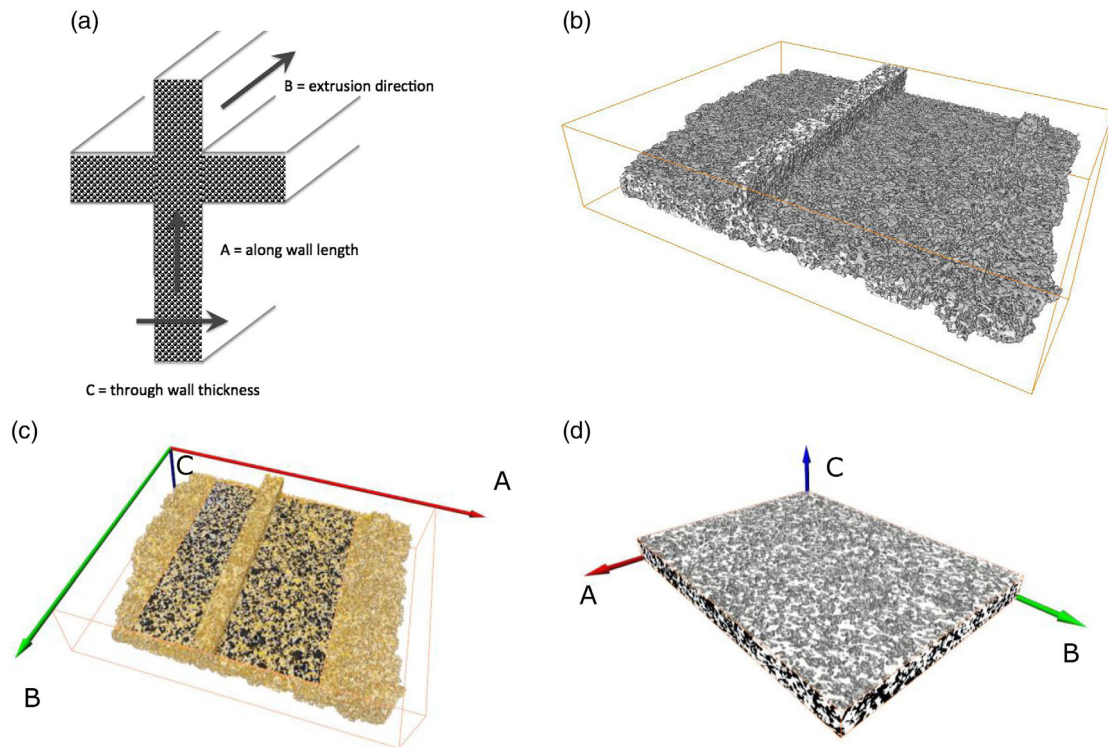


Figure 3. Overview of axis system definition. a) processing axes used to define the samples orientation, b) initial 3D image, c) alignment with processing axes (A red, B green, C blue) and extraction of a fully porous sub-sample (in black), d) resulting segmented volume for Cord_1 sample.

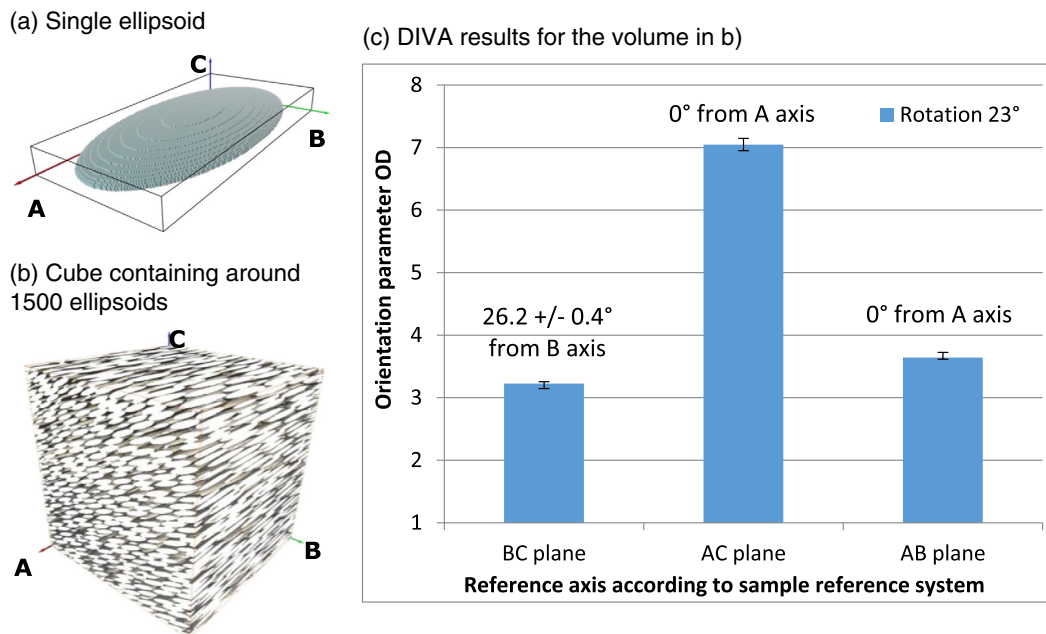


Figure 4. Unit cell of the simulated data a), representative volume element of ellipsoids with a certain orientation, see text, b), and corresponding DIVA orientation parameters c).

randomness), but similar (because of compactness). The results from the DIVA analysis of the simulated volume are presented in Figure 4c. For each plane the orientation parameter in that

plane, O_D , and the direction along which the orientation parameter was obtained (values given above the bar) are given. The maximum orientation parameter is obtained for the AC plane with an

orientation parameter value of 7.0 along the A direction. For the other two planes, the orientation parameters are 3.6 and 3.2 for the AB and BC planes, respectively. In the AB plane, the average pore orientation follows the A direction whereas for the BC plane, it is at 26.2° from the B direction. This value is close to the nominal 23° rotation applied for the 3D image generation. This small discrepancy is explained in Appendix 1.

As shown in the synthetic example, the DIVA analysis provides two types of information. First, it gives for each plane the average ratio between the long and the short axis of the equivalent pore (the orientation parameter O_D), along the three orthogonal axes of the coordinate system. Second, it gives the angular direction of the long axis in the plane where it lies.

The data of the orientation parameter and angular direction, averaged over every plane for each orthogonal orientation, are presented for all DPF materials in Figure 5 and 6, respectively.

For all the cordierite specimens, the maximum value of the orientation parameter is observed in the planes containing the

extrusion direction B (see Figure 5), with higher value in the plane containing the wall thickness (plane BC). This result is not surprising, since it is expected that the shortest dimension (C) should induce a higher degree of alignment, while grains are expected to be able to misalign if the dimension is larger (the wall dimensions are $B > A > C$). The degree of anisotropy is very low within the AB plane (perpendicular to the extrusion axis). Correspondingly (see Figure 6), the long axis of orientation in the planes BC and AB are perfectly aligned with or only a few degrees away from the extrusion axis B. This confirms that the extrusion axis is the preferential direction of the pore space even in 3D. The intensity of this orientation, however, is relatively small (1.15 to 1.35), and it seems that larger porosity p induces less anisotropy (compare Cord_2 and Cord_3 with Cord_4), probably because it is associated with smaller 'pore size'.

For both specimens Cord_3 and Cord_4, for which two samples were taken from 2 perpendicular walls of the DPF, there is a very good agreement between the 2 samples from a given

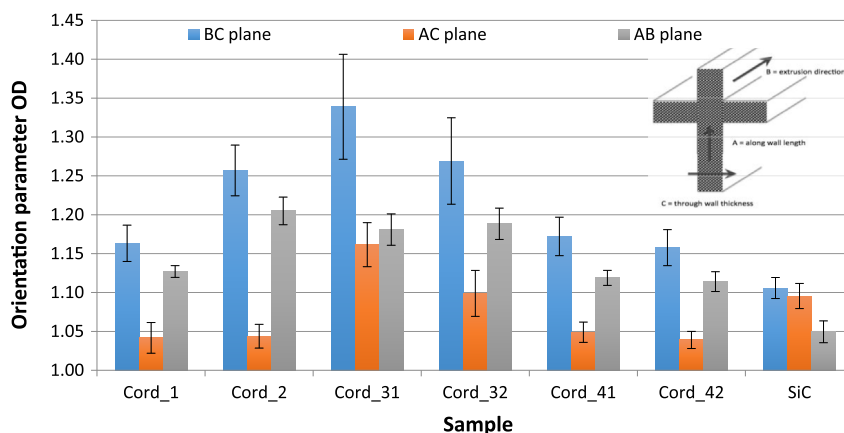


Figure 5. Orientation parameter O_D for each sample plane. BC plane is perpendicular to the wall length, AC plane is perpendicular to the extrusion direction, and AB plane is through the wall thickness.

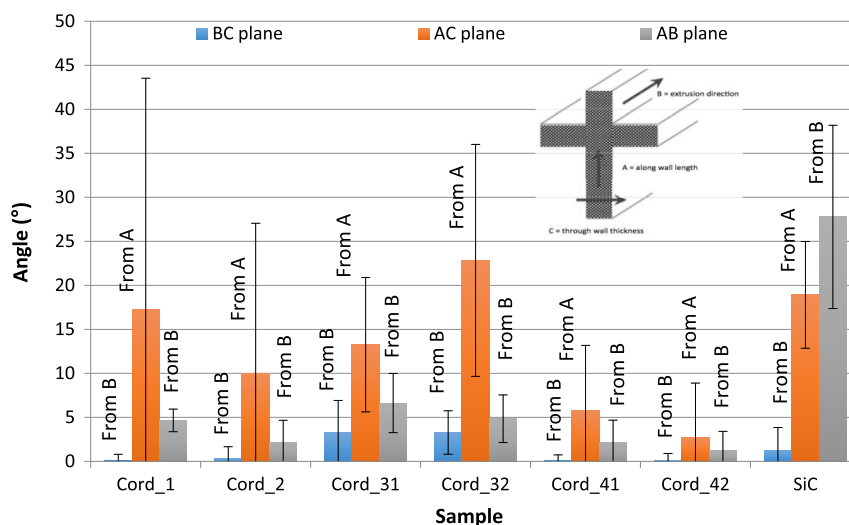


Figure 6. Direction of maximum orientation parameter O_D for each sample plane. BC plane is perpendicular to the wall length, AC plane is perpendicular to the extrusion direction, and AB plane is through the wall thickness.

specimen. This scenario is confirmed by the fact that within the plane BA, a slight misalignment (of the interfaces with respect to the extrusion axis) can be observed. Within the plane of least orientation (AC, i.e., the cross-section of the filter perpendicular to the extrusion axis) a certain angle is present (anyway below $\approx 20^\circ$), but this must be interpreted as a projection of the slight misalignment of the interface with respect to the extrusion axis.

The SiC specimen was chosen to give an example of an isotropic material. It can be noticed that the orientation parameters are similar within the three perpendicular planes and relatively

small, but $O_D \neq 1$. The analysis of the angular preferential orientations within the three planes (Figure 6) shows that the extrusion direction is again the preferred one, but the global orientation is somehow tilted with respect to B. This confirms that overall SiC is much less anisotropic than Cordierite.

5. Discussion

In a companion paper,^[11] we have shown that the morphological anisotropy (pore space geometry) corresponds to the functional

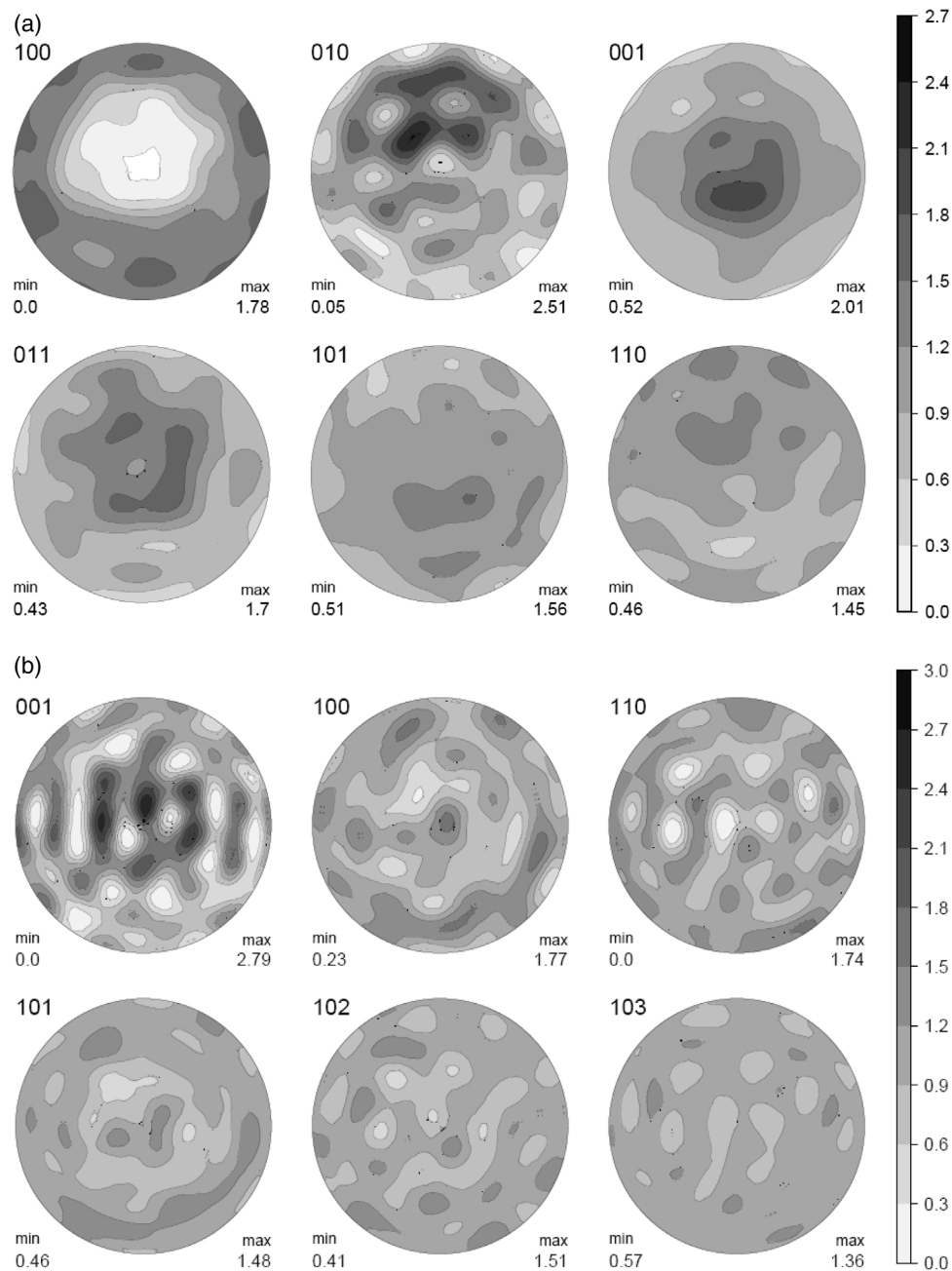


Figure 7. Pole figures of Cord4 a) and SiC b) DPF materials (see also^[21b] for data on Cord_3), as extracted from neutron diffraction measurements on HIPPO, LANSCE, LANL, Los Alamos, NM, USA.

one (permeability). While this is intuitively expected, because the microstructure determines the fluid flow, it also implies that *the necks* of the pore space roughly possess the same orientation as the pore space itself. Since the surface of the two objects (necks and pore structure) is very different, this finding proves to be far from being trivial. It indicates that the extrusion process somehow allows the pore former slurry to squeeze through materials powder particles so that the necks align with the regions of high pore former concentration.

From the results of DIVA, we deduce that the symmetry is orthotropic in Cordierite and close to isotropic in SiC. In Cordierite, as found in,^[21] the degree of *morphological* anisotropy of the microstructure is similar to the intensity of the *crystal* texture. The latter induces anisotropy of the CTE and of the Young's modulus, because of the single crystal anisotropy of such properties. This correlation is strongly influenced by microcracking in DPF materials^[22]; indeed, it has been observed that aluminum titanate (AT) has a much stronger anisotropy of thermal and physical properties than cordierite,^[23] in spite of the fact that its crystal texture is similar. This is due to microcracking, but will not be discussed here, since in cordierite the morphological texture is nearly entirely due to the pore space.^[8b] In **Figure 7**, the crystallographic pole figures of Cordierite and SiC are shown, as determined by neutron diffraction measurements on the instrument HIPPO, LANL, LANSCE, Los Alamos, NM, USA. For Cord_4, the texture is a nearly fiber one with preferred orientation along the [001] axis, with m.r.d. (multiple of random orientation) just above 2. For SiC-6 H (i.e., hexagonal), instead, the texture is nearly random (the

maxima visible in the SiC [001] as well as in Cord_4 [010] pole figures are artifacts of the fit with spherical harmonic functions).

Similar findings can be deduced from the analysis of X-ray refraction radiographs, as done in^[8a] (for details about the experimental technique, see^[8c,24]; a short summary of the salient features of the technique is given in Appendix 2). A comparison of Synchrotron X-ray refraction radiography (SXRR) measurements (carried out on the BAMline at BESSY II, HZB, Berlin, Germany) of Cordierite (taken from^[8a]) and SiC (this work) shows that the pore space in SiC does have some morphological orientation, as shown in the DIVA results above. **Figure 8** shows SXRR pictures (radiographs). In SXRR, a larger signal (brighter gray value) implies the presence of more defects oriented *perpendicularly* to the scattering vector (horizontal in Figure 8a,c, vertical in b and d). Since the pictures acquired with the scattering vector perpendicular to the extrusion direction are indeed brighter, we can deduce that both SiC and Cordierite possess defects elongated preferably *along* the extrusion axis. Interestingly, in SiC the pore space with such preferred orientation is concentrated in a tiny central stripe within the walls. This detail could not have been observed even by Synchrotron XCT and shows the complementarity between SXRR and XCT. The SXRR confirms the expectation that SiC should be more isotropic than cordierite, but also the fact that SiC is not fully isotropic.

It is interesting to note that the observed nonuniformity of the specific surface, when moving from the center of the wall to the intersection regions, was found also in.^[8a,25] This is why in this work we chose for the DIVA analysis only regions belonging to the wall center (between two intersects). Since the analysis is

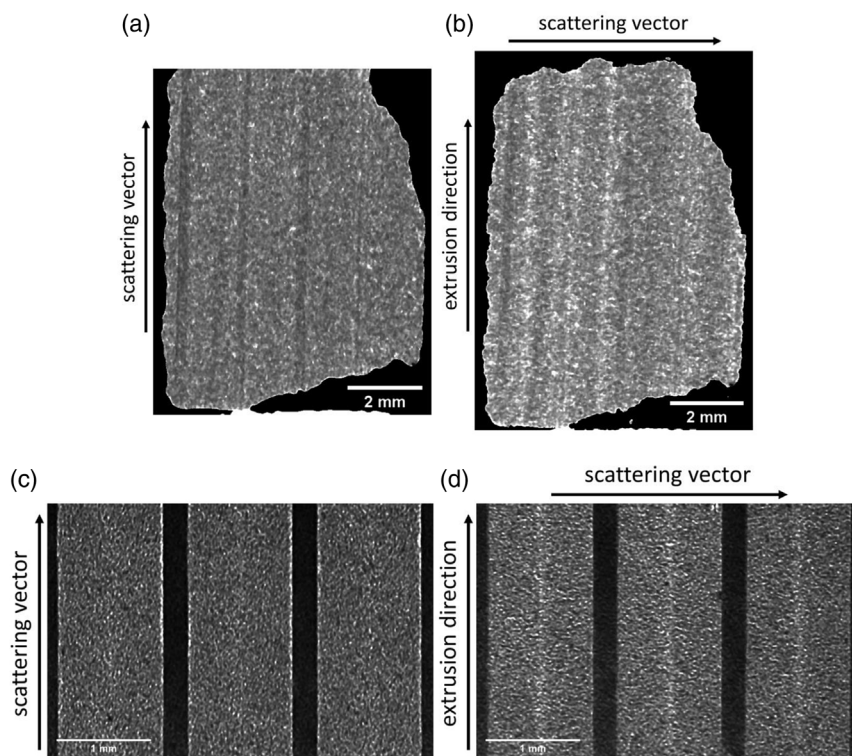


Figure 8. Synchrotron X-ray refraction radiographs of Cordierite (for a, b- see also^[8a]) and SiC (c,d). a,c) show samples with the extrusion direction parallel to the scattering vector (the bisectrix between incident and refracted beam), b,d) show samples with the extrusion direction perpendicular to it.

Table 2. The orientation ratios from x-ray refraction values (normalized to absorption properties)^[35] for SiC and cordierite (Cord_2 in^[11,26]). Such ratios indicate the degree of defect orientation along the extrusion axis. For reference, the results of DIVA and of the autocorrelation function calculations^[11] are also reported.

	SXRR		XCT- DIVA	Autocorrelation (^[11])	
	orientation		Ratio \perp ///	Ratio \perp ///	Ratio \perp ///
	parallel	perpendicular			
SiC	2.35	2.60	1.10	1.10	1.12
Cord_2	1.10 ^[8a]	1.28 ^[8a]	1.16	1.25	1.36

made averaging over the whole a certain volume (see Figure 1), choosing volumes containing different orientation distributions would simply yield an average, and therefore probably lower values of O_D .

Table 2 compares the degree of orientation of Cordierite and SiC, as calculated from DIVA, X-ray refraction radiographs, and the autocorrelation function method, as used in^[11]. It can be observed that for SiC results are extremely consistent among different techniques, while for cordierite a certain discrepancy is present. Such discrepancy can be easily explained by the dimensional nature of the techniques: the SXRR is a 2.5D (i.e., it integrates over the sample thickness), DIVA is a 2D technique, while the autocorrelation function works truly in 3D. The three techniques also work on different sample volumes (much larger for SXRR than the other two). A fully metrological agreement among the techniques is not possible. It is important to remark that the qualitative difference between cordierite and SiC is well caught by all techniques.

We can also conclude that, in the case of both cordierite and SiC DPFs, porosity seems to be dominant over microcracking (see also the analysis in^[26,27]), because the filtration properties possess similar preferential orientation as the microstructure (in other words, the orientation ellipsoids share nearly the same principal axes in the sample coordinates).

It is generally confirmed that cordierite materials possess relatively weak morphological texture, and that increasing porosity (and decreasing the size of the porosity features) actually decreases the degree of anisotropy. In fact, also the thermal and physical properties become less anisotropic^[10].

6. Conclusions

We used a special analysis of 3D XCT data reconstructions to extract quantitative information on the anisotropy of the microstructure (the morphological anisotropy) in Diesel Particulate Filter (DPF) materials, which directly affects their mechanical, thermal, and filtration properties. This analysis, called DIVA, directional interface variance analysis, works on 2D slices of the reconstructed XCT data. We focused our attention on Cordierite and SiC, since their properties mainly depend on the porosity, and are less influenced by microcracking (present only in Cordierite).

We found that in the case of SiC the microstructure is nearly isotropic and that for cordierite the morphological anisotropy of materials is weak and slightly depends on the feature size of the microstructure: the finer the grain and the “pore size” (the latter intended as the quantity that can be determined on 2D slices of XCT reconstructions or SEM pictures), the more isotropic the microstructure. These findings remain in line with the few other studies available in the open literature. Since the microstructure in such materials is dictated by the raw powder and by the pore former particle size, we deduce that controlling those parameters would allow controlling the degree of anisotropy of the physical and mechanical properties of such materials (as well as of the filtration).

Finally, we showed that simple 2D approaches, such as DIVA can be very fast and yield accurate analysis even compared with more sophisticated approaches, such as the autocorrelation function (or the two-point correlation function), if prior knowledge can be used to simplify the problem, as in the case of DPFs (i.e., extruded parts).

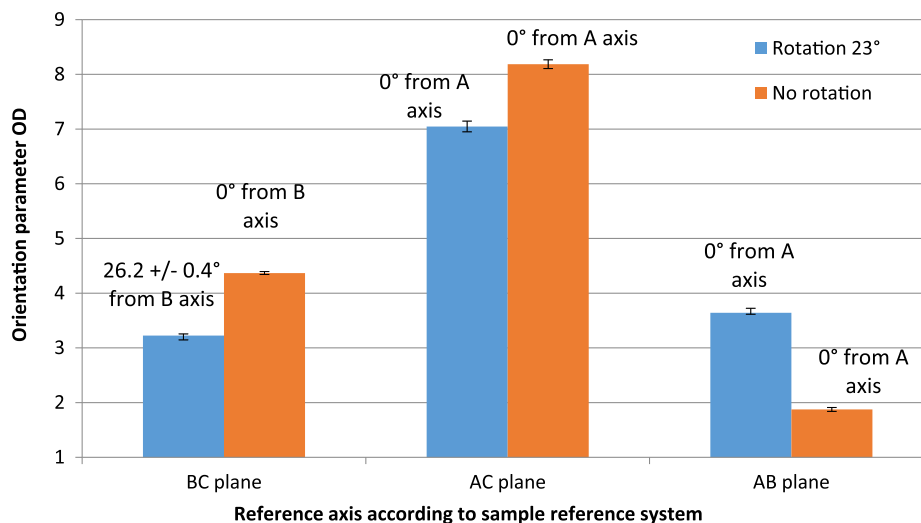


Figure A1. The DIVA orientation parameter for the ellipsoids described in Figure 7a with 23° rotation and no rotation.

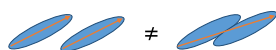


Figure A2. Sketch of the slight change of particle (or pore) orientation in the case a point of contact is present.

Appendices

Appendix A. Considerations on the DIVA Calculation of the Orientation of Overlapping Ellipsoids

In this paragraph, we expand on the difference between the theoretical anisotropy directions on the ideal ellipsoids and those calculated with DIVA (see Figure 4).

If we apply the DIVA calculations to the volume of ellipsoids without rotation we get **Figure A1**. Theoretically, we should get without rotation the following O_D parameters: 5 for A, 10 for B, and 2 for C, while DIVA yields 4.4 for A, 8.2 for B, and 1.9 for C (with the nominal 23° rotation DIVA yields 3.2 for A, 7.0 for B, and 3.6 for C, as well as about 26° rotation from B). In fact, some of the simulated ellipsoids are in contact (see **Figure A2**); they therefore slightly change the overall direction of the medium in each slice (Figure A1). We believe that such “artifact” is actually more representative of the overall orientation of solid with connected porosity, such as our DPFs.

Appendix B. Introduction to X-Ray Refraction

In complete analogy to visible light, the refraction of X-rays occurs at any interface (e.g., pores, cracks, fibers etc. (**Figure A3a**) inside matter (and at outer surfaces). The refraction effect is the stronger, the larger the density (more exactly: the *electron density*) difference between the two materials at the interface. Differently from visible light, the X-ray index of refraction is (slightly) smaller than unity, i.e., the (weak) focussing properties are inverted.^[28] The slight deviation (typically $10^{-7} \dots 10^{-6}$) from unity causes the refraction angles to be very small (some seconds to minutes of arc), so that refraction effects are barely observable in conventional radiology. To this end, X-ray refraction imaging techniques use devices, such as gratings^[29] or crystals^[29] in order to separate the scattered from the primary radiation and to finally generate image contrasts,^[30] alternative to the common absorption contrast.

Three basic facts should be noted: i) Even if the size of individual defects is too small to image them individually (the size is below the spatial resolution of the detector system), their *density* can be quantified in terms of the (integral) specific surface; 2) The technique provides microscopic information (which would otherwise only be available from electron microscopy (EM)) with large field of views (of some mm^2 compared with some μm^2 of EM); and 3) X-ray refraction does not cause an additional attenuation, rather than simply redistributing the incident radiation.

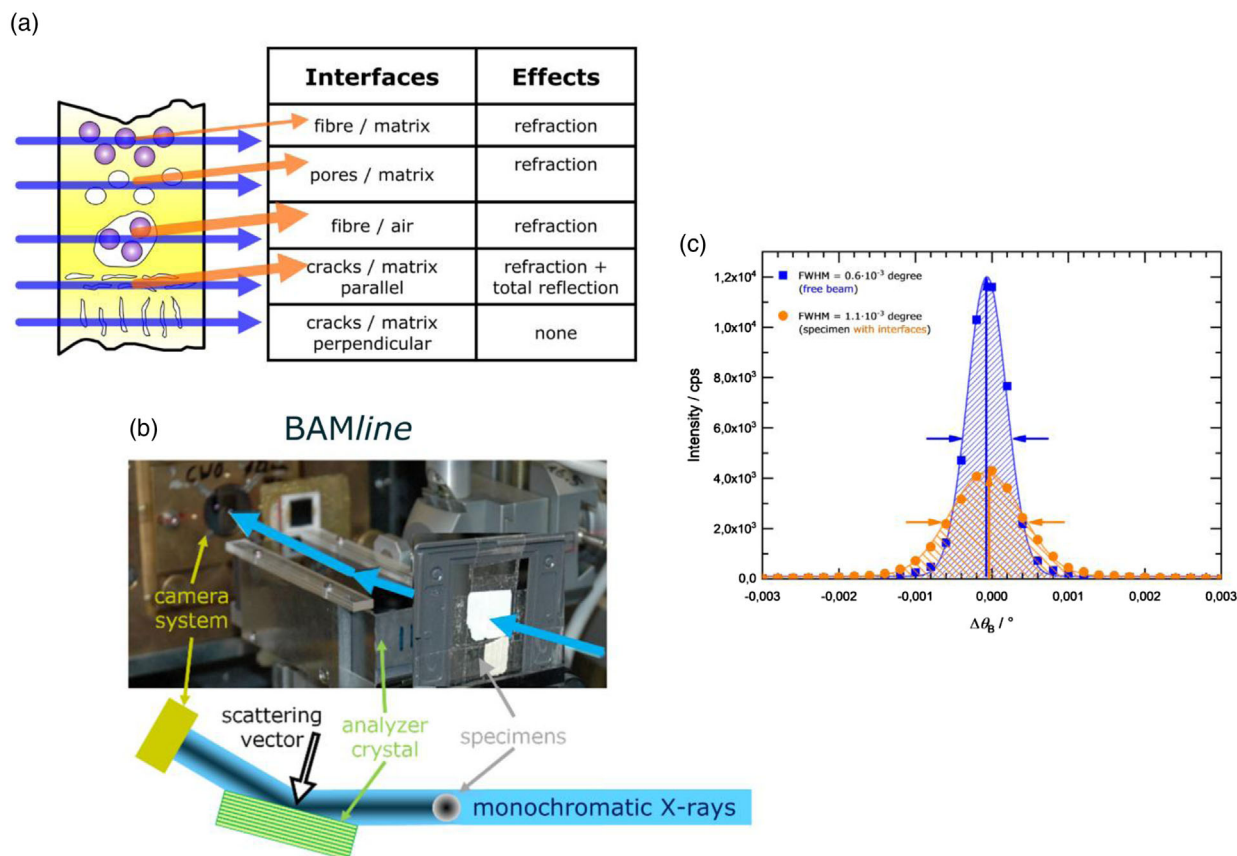


Figure A3. a) Pictorial summary of the applicability of X-ray refraction techniques to different types of defects (microstructures) in materials. b) Sketch and implementation of the diffraction enhanced imaging setup at the BAMline at BESSY II, Berlin. c) Typical RCs rocking curves obtained from DEI measurements of the free beam (“flat field,” blue line) and of a specimen containing microstructures (orange line).

The SXRR images of Figure 8 are obtained from a DEI (Diffraction Enhanced Imaging) setup installed at the BAMline (see Figure A3b) at BESSY II, Berlin.^[16] Its key component is an analyzer single crystal (Silicon), which is tilted around the (111) Bragg reflection, collecting a so-called rocking curve (RC). The crystal is positioned between the sample and the detector. By means of its very narrow peak width (FWHM $\approx 10^{-3}^\circ$, typically), the crystal acts as an angular filter (selector): it selects rays with slightly different directions (i.e., caused by refraction) than the incident radiation (measured as transmission signal). The RC of the free beam (blue line in Figure A3c) serves as reference. The specimen's RC (orange line in Figure A3c) shows on the one hand reduced integral and maximum (due to true absorption) and on the other hand a broadening (due to refraction/scattering). Such broadening is accompanied by an additional reduction of the maximum, but leaving the integral unchanged. Such RCs are recorded and analyzed in each detector (image) pixel. The RCs mentioned above are used to calculate full images of the specific surface (for details of the derivation see e.g.^[24a]).

Beyond the analysis of various ceramic materials,^[1b,8c,13a,26,31] the technique has been shown to be suited to characterize the microstructure of fiber composites,^[32] polymers,^[33] and even metals.^[24,34]

In Figure 8, we exploit the directional sensitivity of X-ray refraction imaging systems. In case of the DEI setup, this sensitivity is predefined by the (analyzer crystal's) scattering plane, which is spanned by the direction of the incident radiation and the (111) reciprocal lattice vector of the analyzer crystal. That is, one obtains signals only from those interfaces, whose normal is nearly parallel to the scattering vector. Interestingly, we remark that since X-ray refraction is sensitive to interfaces, it can be considered the physical analogue of the mathematical DIVA approach, as the later also selects the interface of objects.

Acknowledgements

Open access funding enabled and organized by Projekt DEAL.

Conflict of Interest

The authors declare no conflict of interest.

Data Availability Statement

The data that support the findings of this study are available from the corresponding author upon reasonable request.

Keywords

cordierite, porosity, texture, X-ray computed tomography, X-ray refraction

Received: October 8, 2021

Revised: November 18, 2021

Published online:

[1] a) J. Adler, *Int. J. Appl. Ceram. Tech.* **2005**, *2*, 429; b) G. Bruno, A. M. Efremov, C. P. An, S. Nickerson, *presented at International Conference of Advanced Ceramics and Composites, Daytona Beach,*

- FL*, In S. Widjaja, D. Singh (Eds) *Advances in Bioceramics and Porous Ceramics IV - Ceramic Engineering & Science Proceedings (CESP) 1-5.2.2011* 32.
- [2] a) K. Hamaguchi, K. Kumazawa, S. Asami, *Patent US 5185110 A*, **1993**; b) D. M. Beall, G. A. Merkel, M. J. Murtagh, *Patent US 8999224 B2*, **2015**.
- [3] M. J. Murtagh, D. J. Sherwood, L. S. Socha Jr., *SAE Trans.* **1994**, *103*, 251.
- [4] C. Bubeck, *J. Eur. Ceram. Soc.* **2009**, *29*, 3113.
- [5] G. Bruno, A. M. Efremov, B. Clausen, A. M. Balagurov, V. N. Simkin, B. R. Wheaton, J. E. Webb, D. W. Brown, *Acta Mater.* **2010**, *58*, 1994.
- [6] a) A. Shyam, E. Lara-Curzio, A. Pandey, T. R. Watkins, K. L. More, T. Ohji, *J. Am. Ceram. Soc.* **2012**, *95*, 1682; b) T. Gordon, A. Shyam, E. Lara-Curzio, *J. Am. Ceram. Soc.* **2010**, *93*, 1120.
- [7] A. Lichtner, D. Rousel, D. Jauffrès, C. L. Martin, R. K. Bordia, *J. Am. Ceram. Soc.* **2016**, *99*, 979.
- [8] a) A. Kupsch, A. Lange, M. P. Hentschel, Y. Onel, T. Wolk, A. Staude, K. Ehrig, B. R. Müller, G. Bruno, *J. Ceram. Sci. Technol.* **2013**, *4*, 169; b) Y. Onel, A. Lange, A. Staude, K. Ehrig, A. Kupsch, M. P. Hentschel, T. Wolk, B. R. Müller, G. Bruno, *J. Ceram. Sci. Technol.* **2014**, *5*, 13; c) A. Kupsch, B. R. Müller, A. Lange, G. Bruno, *J. Eur. Ceram. Soc.* **2017**, *37*, 1879.
- [9] a) S.-H. Leigh, C. C. Berndt, *Acta Mater* **1999**, *47*, 1575; b) A. P. Roberts, E. J. Garboczi, *J. Am. Ceram. Soc.* **2000**, *83*, 3041.
- [10] G. Bruno, A. M. Efremov, C. P. An, B. R. Wheaton, D. J. Hughes, *J. Mater. Sci.* **2012**, *47*, 3674.
- [11] D. Bernard, F. Léonard, E. Plougonven, G. Bruno, *Philos. Mag.* **2020**, *100*, 2802.
- [12] S. Nickerson, Y. Shu, D. Zhong, C. Könke, A. Tandia, *Acta Mater.* **2019**, *172*, 121.
- [13] a) B. R. Müller, R. C. Cooper, A. Lange, A. Kupsch, M. Wheeler, M. P. Hentschel, A. Staude, A. Pandey, A. Shyam, G. Bruno, *Acta Mater* **2018**, *144*, 627; b) C. Chen, B. R. Müller, C. Prinz, J. Stroh, I. Feldmann, G. Bruno, *J. Eur. Ceram. Soc.* **2020**, *40*, 1592.
- [14] a) M. Kachanov, J. W. Hutchinson, T. Y. Wu, in *Advances in Applied Mechanics*, Vol. 30 (Eds: J. W. Hutchinson, T. Y. Wu), Elsevier, Amsterdam **1993**, p. 259; b) I. Sevostianov, M. Kachanov, *Int. J. Eng. Sci.* **2008**, *46*, 211.
- [15] a) G. Bruno, A. Efremov, B. Wheaton, I. Bobrikov, V. G. Simkin, S. Mixture, *J. E. Ceram. Soc.* **2010**, *30*, 2555; b) A. Doncieux, K. Ninomiya, N. Ishizawa, T. Ota, M. Huger, *Annu. Rep. - Adv. Ceram. Res. Cent., Nagoya Inst. Technol.* **2016**, *5*, 1.
- [16] a) W. Görner, M. P. Hentschel, B. R. Müller, H. Riesemeier, M. Krumrey, G. Ulm, W. Diete, U. Klein, R. Frahm, *Nucl. Instrum. Methods Phys. Res., Sect. A* **2001**, *467–468*, 703; b) A. Rack, S. Zabler, B. R. Müller, H. Riesemeier, G. Weidemann, A. Lange, J. Goebbels, M. Hentschel, W. Görner, *Nucl. Instrum. Methods Phys. Res., Sect. A* **2008**, *586*, 327.
- [17] A. M. Al-Falahat, A. Kupsch, M. P. Hentschel, A. Lange, N. Kardjilov, H. Markötter, I. Manke, *Rev. Sci. Instrum.* **2019**, *90*, 125108.
- [18] A. Lange, M. P. Hentschel, A. Kupsch, B. R. Müller, *Int. J. Mater. Res.* **2012**, *103*, 174.
- [19] G. Bruno, A. M. Efremov, C. An, S. Nickerson, *Adv. Bioceram. Porous Ceram. IV: Ceram. Eng. Sci. Proc.* **2011**, 32.
- [20] G. Bruno, A. M. Efremov, A. N. Levandovskiy, B. Clausen, *J. Mater. Sci.* **2011**, *46*, 161.
- [21] a) G. Bruno, S. Vogel, *J. Am. Ceram. Soc.* **2008**, *91*, 2646; b) G. Bruno, S. Vogel, *J. Appl. Cryst.* **2017**, *50*, 749.
- [22] G. Bruno, A. M. Efremov, B. R. Wheaton, J. E. Webb, *Acta Mater.* **2010**, *58*, 6649.
- [23] G. Bruno, A. M. Efremov, A. N. Levandovskiy, I. Pozdnyakova, D. J. Hughes, B. Clausen, *Mater. Sci. Forum* **2010**, *652*, 191.
- [24] a) J. Nellesen, R. Laquai, B. R. Müller, A. Kupsch, M. P. Hentschel, N. B. Anar, E. Soppa, W. Tillmann, G. Bruno, *J Mater Sci* **2018**, *53*,

- 6021; b) R. Laquai, B. Müller, G. Kasperovich, G. Requena, J. Haubrich, G. Bruno, *Mater. Perform. Charact.* **2020**, 9, 82.
- [25] A. M. Efremov, G. Bruno, B. R. Wheaton, *J. Eur. Ceram. Soc.* **2011**, 31, 281.
- [26] A. Kupsch, A. Lange, M. P. Hentschel, Y. Onel, T. Wolk, A. Staude, K. Ehrig, B. R. Müller, G. Bruno, *J. Ceram. Sci. Technol.* **2013**, 4, 169.
- [27] Y. Onel, A. Lange, A. Staude, K. Ehrig, A. Kupsch, M. P. Hentschel, T. Wolk, B. R. Müller, G. Bruno, *J. Ceram. Sci. Technol.* **2013**, 05, 13.
- [28] S. Evsevlev, B. R. Müller, A. Lange, A. Kupsch, *Nucl. Instrum. Methods Phys. Res., Sect. A* **2019**, 916, 275.
- [29] a) F. Pfeiffer, T. Weitkamp, O. Bunk, C. David, *Nat. Phys.* **2006**, 2, 258; b) A. Olivo, R. Speller, *Phys. Med. Biol.* **2007**, 52, 6555.
- [30] a) M. Bech, A. Tapfer, A. Velroyen, A. Yaroshenko, B. Pauwels, J. Hostens, P. Bruyndonckx, A. Sasov, F. Pfeiffer, *Sci. Rep.* **2013**, 3, 3; b) F. Arfelli, A. Astolfo, L. Rigon, R. H. Menk, *Sci. Rep.* **2018**, 8, 14; c) H. Chen, B. Liu, L. M. Zhao, K. Ren, Z. L. Wang, *Chin. Phys. B* **2021**, 30, 5.
- [31] A. Kupsch, R. Laquai, B. R. Müller, S. Paciornik, J. Horvath, K. Tushtev, K. Rezwani, G. Bruno, *Adv. Eng. Mater.* **2021**, 2100763 <https://doi.org/10.1002/adem.202100763>.
- [32] a) A. Kupsch, V. Trappe, B. R. Müller, G. Bruno, *Evolution of CFRP stress cracks observed by in-situ X-ray refractive imaging* IOP Conf. Series: Materials Science and Engineering **2020**, 942, 012035; b) A. P. Soares, D. Baum, B. Hesse, A. Kupsch, B. R. Müller, P. Zaslansky, *Dent. Mater.* **2021**, 37, 201.
- [33] a) M. Erdmann, A. Kupsch, B. R. Müller, M. P. Hentschel, U. Niebergall, M. Bohning, G. Bruno, *J. Mater. Sci.* **2019**, 54, 11739; b) D. Schob, R. Roszak, I. Sagradov, H. Sparr, M. Ziegenhorn, A. Kupsch, F. Leonard, B. R. Müller, G. Bruno, *Arch. Mech.* **2019**, 71, 507; c) D. Schob, I. Sagradov, R. Roszak, H. Sparr, R. Franke, M. Ziegenhorn, A. Kupsch, F. Leonard, B. R. Müller, G. Bruno, *Eng. Fract. Mech.* **2020**, 229.
- [34] R. Laquai, B. R. Müller, J. A. Schneider, A. Kupsch, G. Bruno, *Metall. Mater. Trans. A-Phys. Metall. Mater. Sci.* **2020**, 51, 4146.
- [35] M. P. Hentschel, A. Lange, B. R. Müller, J. Schors, K. W. Harbich, *Materialprüfung* **2000**, 42, 217.